

# Quasiparticle Interference in the Unconventional Metamagnetic Compound $\text{Sr}_3\text{Ru}_2\text{O}_7$

Wei-Cheng Lee,<sup>1,\*</sup> D. P. Arovas,<sup>1,†</sup> and Congjun Wu<sup>1,‡</sup>

<sup>1</sup>*Department of Physics, University of California, San Diego, California, 92093, USA*

(Dated: October 4, 2018)

Quasiparticle interference (QPI) in spectroscopic imaging scanning tunneling microscopy provides a powerful method to detect orbital band structures and orbital ordering patterns in transition metal oxides. We use the  $T$ -matrix formalism to calculate the QPI spectra for the unconventional metamagnetic system of  $\text{Sr}_3\text{Ru}_2\text{O}_7$  with a  $t_{2g}$ -orbital band structure. A detailed tight-binding model is constructed accounting for features such as spin-orbit coupling, bilayer splitting, and the staggered rotation of the RuO octahedra. The band parameters are chosen by fitting the calculated Fermi surfaces with those measured in the angular-resolved photo-emission spectroscopy experiment. The calculated quasiparticle interference at zero magnetic field exhibits a hollow square-like feature arising from the nesting of the quasi-1d  $d_{xz}$  and  $d_{yz}$  orbital bands, in agreement with recent measurements by J. Lee *et al.* (Nature Physics **5**, 800 (2009)). Rotational symmetry breaking in the nematic metamagnetic state also manifests in the quasi-particle interference spectra.

PACS numbers: 68.37.Ef, 61.30.Eb, 75.10.-b, 71.10.Ay

## I. INTRODUCTION

The physics of transition metal oxides is characterized by a rich interplay among the lattice, charge, spin and orbital degrees of freedom<sup>1-4</sup>. Various exotic phenomena, such as metal-insulator transitions and colossal magnetoresistance occur in orbitally active compounds with partially filled  $d$  or  $f$ -shells. In the literature many Mott-insulating orbital systems (*e.g.*,  $\text{La}_{1-x}\text{Sr}_x\text{MnO}_3$ ,  $\text{La}_4\text{Ru}_2\text{O}_{10}$ ,  $\text{LaTiO}_3$ ,  $\text{YTiO}_3$ ,  $\text{KCuF}_3$ )<sup>5-8</sup> have been extensively studied, and both orbital ordering and orbital excitations have been observed. Significant developments in orbital physics have also been made recently in cold atom optical lattice systems. In particular, strongly correlated  $p$ -orbital bands filled with both bosons and fermions provides a new perspective on orbital physics which has not yet been explored in the solid state context<sup>9-15</sup>. In contrast, most  $p$ -orbital solid state systems exhibit only relatively weak correlations.

Metallic orbital systems, such as strontium ruthenates and iron-pnictide superconductors, have received a great deal of attention of late. Their Fermi surfaces are characterized by hybridized  $t_{2g}$ -orbital bands, *i.e.*, the eigen-orbital admixture of the Bloch state varies around a connected region of the Fermi surface. Orbital ordering in such systems corresponds to a preferred occupation along particular directions on the Fermi surface, and thus breaks the lattice point group symmetry<sup>16-20</sup>. As a result, orbital ordering is equivalent to the anisotropic Pomeranchuk instability of Fermi liquids.

Pomeranchuk instabilities are a large class of Fermi surface instabilities in the particle-hole channel with non- $s$ -wave symmetry, which can be decomposed into both density and spin-channel instabilities. The density channel instabilities often result in uniform but anisotropic (nematic) electron liquid states<sup>21-35</sup>. These instabilities have been studied in the context of doped Mott insulators<sup>36</sup>, high  $T_c$  materials<sup>30,36</sup>, and quantum Hall systems with nearly half-filled Landau levels<sup>37,38</sup>. The spin

channel Pomeranchuk instabilities are a form of “*unconventional magnetism*” analogous to unconventional superconductivity<sup>21,31,32,39-44</sup>. The instabilities result in new phases of matter, dubbed  $\beta$  and  $\alpha$ , which respectively are counterparts to the  $B$  (isotropic) and  $A$  (anisotropic) phases of  $^3\text{He}$ <sup>41,42</sup>. Systematic studies of the ground state properties and collective excitations in both the  $\alpha$  and  $\beta$ -phases have been performed in Refs. [41] and [42].

The  $t_{2g}$ -orbital system of the bilayer ruthenate  $\text{Sr}_3\text{Ru}_2\text{O}_7$  exhibits an unconventional anisotropic (nematic) metamagnetic state<sup>45-47</sup>, which has aroused much attention<sup>29,32,48-55</sup>.  $\text{Sr}_3\text{Ru}_2\text{O}_7$  is a metallic itinerant system with  $\text{RuO}_2$  ( $ab$ ) planes. It is paramagnetic at zero magnetic field, and below 1K develops two consecutive metamagnetic transitions in an external magnetic field  $B$  perpendicular to the  $ab$ -plane at 7.8 and 8.1 Tesla. Between two metamagnetic transitions, the resistivity measurements show a strong spontaneous in-plane anisotropy along the  $a$  and  $b$ -axis, with no noticeable lattice distortions. This feature, which is presumed to be of electronic order, may be interpreted as due to nematicity resulting from an anisotropic distortion of the Fermi surface of the majority spin polarized by the external magnetic field<sup>46</sup>. Essentially this reflects a mixture of the  $d$ -wave Pomeranchuk instabilities in both density and spin channels. Recently, different microscopic theories have been constructed based on the quasi-1d bands of  $d_{xz}$  and  $d_{yz}$  by two of us<sup>19</sup> and also by Raghu *et al.*<sup>20</sup>, and based on the 2d-band of  $d_{xy}$  by Puetter *et al.*<sup>55</sup>. In our theory, the unconventional (nematic) magnetic ordering was interpreted as orbital ordering among the  $d_{xz}$  and  $d_{yz}$ -orbitals.

Unlike charge and spin, orbital ordering is often difficult to measure particularly in metallic systems. Recently, the technique of spectroscopic imaging scanning tunneling microscopy (SI-STM) has been applied to the active  $d$ -orbital systems of  $\text{Sr}_3\text{Ru}_2\text{O}_7$ <sup>56</sup> and  $\text{Ca}(\text{Fe}_{1-x}\text{Co}_x)_2\text{As}_2$ <sup>57</sup>. The SI-STM quasi-particle inter-

ference (QPI) analysis is an important tool to study competing orders in strongly correlated systems<sup>58–60</sup>, and has recently been applied to analyze the orbital band structure and orbital ordering in such systems. The QPI pattern in  $\text{Sr}_3\text{Ru}_2\text{O}_7$  exhibits characteristic square box-like features<sup>56</sup>, and that of  $\text{Ca}(\text{Fe}_{1-x}\text{Co}_x)_2\text{As}_2$  exhibits strong two-fold anisotropy<sup>57</sup>. In both cases, the QPI spectra are associated with the quasi-one dimensional  $d_{xz}$  and  $d_{yz}$ -bands.

In a previous paper<sup>61</sup>, two of us performed a theoretical analysis showing that QPI provides a sensitive method to detect orbital degree of freedom and orbital ordering in the quasi-1d  $d_{xz}$  and  $d_{yz}$  bands. The  $T$ -matrix acquires momentum-dependent form factors which extinguish certain QPI wavevectors and result in crossed stripe features in the Fourier-transformed STM images. The orbital ordering is reflected in the nematic distortion of the stripe QPI patterns. These results are in qualitative agreement with recent experiments<sup>56,57</sup>.

In this article, we perform a detailed theoretical study of the QPI spectra in  $\text{Sr}_3\text{Ru}_2\text{O}_7$ , based on its  $t_{2g}$ -band structure. Various realistic features are taken into account to construct the tight-binding model, including the bilayer structure, the staggered rotation of the RuO octahedra, and the on-site spin-orbit coupling. In addition, in order to account for the fact that STM is a surface sensitive probe, a potential bias is added between the top and bottom layers. Our calculation clearly shows the square box-like feature arising from the QPI in the  $d_{xz}$  and  $d_{yz}$ -bands, which agrees well with the experimental data in Ref. [56]. Furthermore, we predict a reduction of the four-fold rotational ( $C_4$ ) symmetry to two-fold ( $C_2$ ) in the unconventional (nematic) metamagnetic states.

This article is organized as follows. In section II, we construct a detailed tight-binding model to describe the bilayer  $t_{2g}$ -band structures. We choose the model parameters so as to fit the experimentally measured Fermi surface from angular resolved photon emission spectroscopy (ARPES). In section III, we present the  $T$ -matrix method for the QPI spectra for the multi-orbital band systems. The fact that the experimentally measured QPI is predominantly due to the top layer is carefully taken into account. In section IV, we show the calculated QPI patterns and a comparison with experiments. Predictions are then made for the QPI pattern in the presence of the nematic orbital ordering. Conclusions are given in section VI.

## II. TIGHT-BINDING MODEL FOR THE BILAYER $t_{2g}$ -ORBITAL BAND

The bilayer ruthenate compound  $\text{Sr}_3\text{Ru}_2\text{O}_7$  has a quasi-two dimensional layered structure. Its band structure in the vicinity of the Fermi level is dominated by the  $t_{2g}$ -orbitals on the Ru sites, and is complicated by the on-site spin-orbit coupling and the staggered rotation

pattern of the RuO octahedra. In this section, we derive

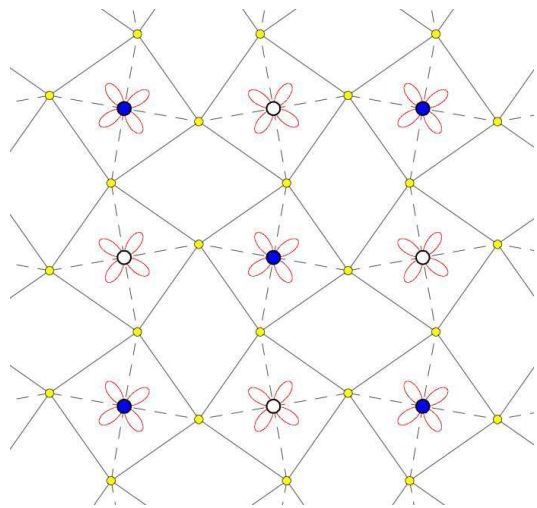


FIG. 1: (Color online) The lattice structure in a single layer of  $\text{Sr}_3\text{Ru}_2\text{O}_7$ . The small yellow circle represents the octahedra oxygens which rotate about  $6.8^\circ$  (the angle in the plot is a little exaggerated) with respect to the  $z$  axis on the Ru sites. The red curves show the orientations of the Ru  $d_{xy}$  orbitals. Because the direction of the rotation is opposite for nearest neighbor Ru sites, two types of the sublattice are identified as A (blue dot) and B (white dot). The direction of rotation is also opposite from bottom to top layers, leading to the switch of the sublattices A and B in different layers.

the form of the tight-binding model based on symmetry considerations.

The lattice structure of one layer of  $\text{Sr}_3\text{Ru}_2\text{O}_7$  is plotted in Fig. 1, showing the rotation of the octahedra oxygens with opposite directions between neighboring Ru sites. Neutron diffraction measurement<sup>62</sup> indicated that the rotation directions are reversed on the top and bottom layers. This staggered rotation pattern leads to not only a unit cell doubling but also additional hoppings which are absent in a perfect square lattice, and it is crucial to take this detail into account in constructing a realistic tight-binding model. To make the discussion simple, we divide the hopping terms into four parts: the in-plane hoppings existing without rotations  $H_1^{\text{INTRA}}$ , the in-plane hoppings induced by the rotations  $H_2^{\text{INTRA}}$ , the inter-layer hoppings existing without the rotations  $H_1^{\text{INTER}}$ , and finally the inter-layer hoppings induced by the rotations  $H_2^{\text{INTER}}$ .

### A. Uniform hopping terms without RuO octahedron rotation

The Hamiltonian for  $H_1^{\text{INTRA}}$  has been presented in Refs. [20] and [55]. Following Ref. [55],  $H_1^{\text{INTRA}}$  reads

$$\begin{aligned}
H_1^{\text{INTRA}} = \sum_{\vec{r}, s, a} \left\{ & -t_1 \left[ d_{s,a}^{xz \dagger}(\vec{r} + \hat{x}) d_{s,a}^{xz}(\vec{r}) + d_{s,a}^{yz \dagger}(\vec{r} + \hat{y}) d_{s,a}^{yz}(\vec{r}) \right] - t_2 \left[ d_{s,a}^{yz \dagger}(\vec{r} + \hat{x}) d_{s,a}^{yz}(\vec{r}) + d_{s,a}^{xz \dagger}(\vec{r} + \hat{y}) d_{s,a}^{xz}(\vec{r}) \right] \right. \\
& - t_3 \left[ d_{s,a}^{xy \dagger}(\vec{r} + \hat{x}) d_{s,a}^{xy}(\vec{r}) + d_{s,a}^{xy \dagger}(\vec{r} + \hat{y}) d_{s,a}^{xy}(\vec{r}) \right] - t_4 \left[ d_{s,a}^{xy \dagger}(\vec{r} + \hat{x} + \hat{y}) d_{s,a}^{xy}(\vec{r}) + d_{s,a}^{xy \dagger}(\vec{r} + \hat{x} - \hat{y}) d_{s,a}^{xy}(\vec{r}) \right] \\
& - t_5 \left[ d_{s,a}^{xy \dagger}(\vec{r} + 2\hat{x}) d_{s,a}^{xy}(\vec{r}) + d_{s,a}^{xy \dagger}(\vec{r} + 2\hat{y}) d_{s,a}^{xy}(\vec{r}) \right] \\
& \left. - t_6 \left[ d_{s,a}^{yz \dagger}(\vec{r} + \hat{x} - \hat{y}) d_{s,a}^{yz}(\vec{r}) - d_{s,a}^{yz \dagger}(\vec{r} + \hat{x} + \hat{y}) d_{s,a}^{yz}(\vec{r}) \right] \right\} + \text{H.c.} \\
& - V_{xy} d_{s,a}^{xy \dagger}(\vec{r}) d_{s,a}^{xy}(\vec{r}) + 2\lambda \sum_{\vec{r}} \vec{L}(\vec{r}) \cdot \vec{S}(\vec{r}) , \tag{1}
\end{aligned}$$

which includes longitudinal ( $t_1$ ) and transverse ( $t_2$ ) hopping for the the  $d_{xz}$  and  $d_{yz}$  orbitals, respectively, as well as are nearest neighbor ( $t_3$ ), next-nearest neighbor ( $t_4$ ), and next-next-nearest neighbor ( $t_5$ ) hopping for the  $d_{xy}$  orbital. The summation indices  $\vec{r}$ ,  $s$ , and  $a$  refer to the position of Ru sites, the spin, and the layer indices. While symmetry forbids nearest-neighbor hopping between different  $t_{2g}$  orbitals in a perfect square lattice, due to the rotation of the oxygen octahedra, we include a term describing hopping between  $d_{xz}$  and  $d_{yz}$  orbitals on next-nearest neighbor sites ( $t_6$ ). In each layer, the Ru sites  $\vec{r}$  lie on a square lattice; we set the lattice constant to unity throughout.

We assume  $|t_3| \approx |t_1| \gg |t_2|$ , in accordance with the 2d nature of  $d_{xy}$  and quasi-1d nature of  $d_{yz}$  and  $d_{xz}$  orbitals. While the hopping integral  $t_2$  arises from the direct overlap of the Wannier wavefunctions for the  $t_{2g}$  bands, the major contributions to  $t_1$  and  $t_3$  are from the hopping through the oxygen  $2p$ -orbitals. The corresponding hopping processes are sketched in Fig. 2. The signs of nearest neighbor hopping integrals  $t_1$  and  $t_3$  can be obtained from the second order perturbation theory:

$$-t_1 = \frac{t_{pd}(-t_{pd})}{E_d - E_p} < 0. \tag{2}$$

where  $t_{pd}$  is defined as the hopping integral between the ruthenium  $d_{xz}$  orbital at position  $\vec{r}$  and the oxygen  $p_z$  orbital at position  $\vec{r} + \frac{1}{2}\hat{x}$ , which is identical to that between the Ru  $d_{yz}$  orbital at  $\vec{r}$  and the O  $p_z$  orbital at  $\vec{r} + \frac{1}{2}\hat{x}$ . To get  $t_3$ , replace the  $d_{xz}$  or  $d_{yz}$  orbital with the  $d_{xy}$  orbital. The sign follows from the fact that  $E_d - E_p > 0$ . As for  $t_2$ , since it results from a direct overlap, as shown in Fig. 2(b), we have  $t_2 > 0$ . Their magnitudes are estimated as  $t_1 \approx t_3 \approx 300$  meV and  $t_2/t_1 \approx 0.1$  from a fitting of LDA calculations on  $\text{Sr}_2\text{RuO}_4$ <sup>63,64</sup>. For the long distance hoppings  $t_{4,5}$  whose magnitudes are smaller, their values are put by hand for later convenience. The on-site potential for the  $d_{xy}$  orbital  $V_{xy}$  is introduced to take into account the splitting of the  $d_{yz}$  and  $d_{xz}$  states relative to the  $d_{xy}$  states which was found in LDA calculations<sup>65</sup>. We take  $V_{xy}/t_1 = 0.3$ .

The last term in  $H_1^{\text{INTRA}}$  describes the on-site spin-orbit coupling, the energy scale of which is estimated in Ref. [66] to be  $\lambda = 90$  meV, based on a first principles study of  $\text{Sr}_2\text{RuO}_4$ . This term couples the  $d_{xy}$  and  $d_{xz,yz}$  orbitals. Truncated in the three-dimensional subspace of  $t_{2g}$  orbitals spanned by  $(d_{yz}, d_{xz}, d_{xy})$ , the matrix form of the  $\vec{L}$  operators reads

$$\begin{aligned}
L_x = \begin{pmatrix} 0 & 0 & 0 \\ 0 & 0 & i \\ 0 & -i & 0 \end{pmatrix}, \quad L_y = \begin{pmatrix} 0 & 0 & -i \\ 0 & 0 & 0 \\ i & 0 & 0 \end{pmatrix} \\
L_z = \begin{pmatrix} 0 & i & 0 \\ -i & 0 & 0 \\ 0 & 0 & 0 \end{pmatrix}. \tag{3}
\end{aligned}$$

It is important to note that, unlike the usual angular momentum operators, the truncated matrices satisfy a different commutation relation, *i.e.*

$$[L_i, L_j] = -i\epsilon_{ijk} L_k. \tag{4}$$

The Hamiltonian Eq. 1 is expressed in momentum space as

$$H_1^{\text{INTRA}} = \sum_{\vec{k}, a} \left[ \psi_{s,a}^\dagger(\vec{k}) \hat{A}_s(\vec{k}) \psi_{s,a}(\vec{k}) + \text{H.c.} \right] \tag{5}$$

where  $\psi_{s,a}(\vec{k})$  is defined as a 3-component spinor as  $\psi(\vec{k}) = [d_{s,a}^{yz}(\vec{k}), d_{s,a}^{xz}(\vec{k}), d_{-s,a}^{xy}(\vec{k})]^T$  and  $d_{s,a}^\alpha(\vec{k})$  annihilates an electron with orbital  $\alpha$  and spin polarization  $s$  at momentum  $\vec{k}$  in the top ( $a = t$ ) or bottom ( $a = b$ ) layer. The matrix kernel  $\hat{A}_s(\vec{k})$  in Eq. 5 is

$$\hat{A}_s(\vec{k}) = \begin{pmatrix} \epsilon_k^{yz} & \epsilon_k^{\text{off}} + is\lambda & -s\lambda \\ \epsilon_k^{\text{off}} - is\lambda & \epsilon_k^{xz} & i\lambda \\ -s\lambda & -i\lambda & \epsilon_k^{xy} \end{pmatrix}, \tag{6}$$

where the dispersions for the  $d_{yz}$ ,  $d_{xz}$ , and  $d_{xy}$  bands are

$$\begin{aligned}
\epsilon_k^{yz} &= -2t_2 \cos k_x - 2t_1 \cos k_y, \\
\epsilon_k^{xz} &= -2t_1 \cos k_x - 2t_2 \cos k_y, \\
\epsilon_k^{xy} &= -2t_3 (\cos k_x + \cos k_y) - 4t_4 \cos k_x \cos k_y \\
&\quad - 2t_5 (\cos 2k_x + \cos 2k_y) - V_{xy}, \tag{7}
\end{aligned}$$

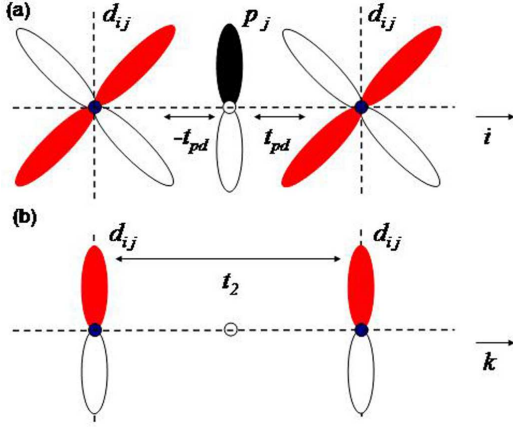


FIG. 2: (Color online) Hopping processes for (a)  $t_1$  and  $t_3$  (b)  $t_2$ . For each  $i, j, k$ , it can be  $\hat{x}, \hat{y}, \hat{z}$ , but  $i \neq j \neq k$ . (a) The hopping processes described by  $t_1$  and  $t_3$  are assisted by the  $p$  orbital of oxygens. (b) The hopping process described by  $t_2$  is through the direct overlap between two identical orbitals on the nearest-neighbor Ru sites without going through the oxygen, thus it is much weaker than  $t_1$  and  $t_3$ .

and

$$c_k^{\text{off}} = -4t_6 \sin k_x \sin k_y. \quad (8)$$

As for  $H_1^{\text{INTER}}$ , since the wavefunction of the  $d_{xy}$  orbital lies largely within the  $ab$ -plane, its inter-layer hopping is assumed negligible in comparison to that for the  $d_{xz}$  and  $d_{yz}$ -orbitals. This leads to

$$H_1^{\text{INTER}} = -t_{\perp} \sum_{\alpha=xz,yz} \sum_{\vec{k}, \vec{s}} \left\{ d_{s,t}^{\alpha \dagger}(\vec{k}) d_{s,b}^{\alpha}(\vec{k}) + \text{H.c.} \right\} \quad (9)$$

### B. Staggered intra-plane hopping induced by staggered rotation of RuO octahedron

In this subsection, we study the additional intra-plane hoppings induced by the staggered rotation of the octahedron oxygens. The leading effect of this rotation is to enable hopping between different orbitals on nearest neighbor sites. A spin-dependent hopping between  $d_{xy}$  band due to the spin-orbit coupling has been discussed in Ref. [67]. In the following, we neglect the weak breaking of reflection symmetry of each  $ab$  plane due to the bilayer structure. Since  $d_{yz}$  and  $d_{xz}$  are odd and  $d_{xy}$  is even under this reflection  $z \rightarrow -z$ , the inter-orbital hoppings between  $d_{yz}$  (or  $d_{xz}$ ) and  $d_{xy}$  are still zero under this assumption. Therefore we only need to consider the hopping between  $d_{yz}$  and  $d_{xz}$  orbitals. In the following, we will show that this inter-orbital hopping has staggered signs in the real space, which causes a unit cell doubling as seen in LDA calculations<sup>65</sup> and ARPES experiment<sup>52</sup>.

We start with the hopping along the  $\hat{x}$ -direction with spin  $s$  and in the layer  $a$ , and consider the hopping between  $d^{yz}$  and  $d^{xz}$  orbitals illustrated in Fig. 3(a) as

$$-t_{\text{INT}} \left( d_{s,a}^{yz \dagger}(\vec{r}) d_{s,a}^{xz}(\vec{r} - \hat{x}) + \text{H.c.} \right). \quad (10)$$

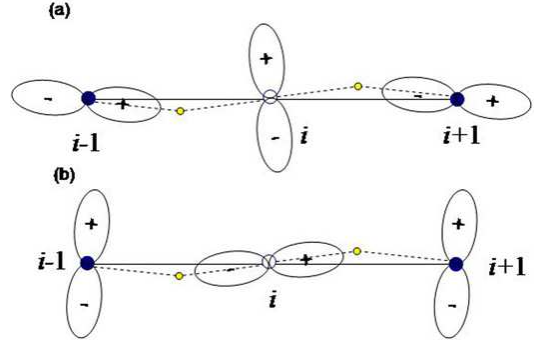


FIG. 3: (Color online) The Wannier wavefunctions of the  $d_{yz}$  and  $d_{xz}$  with the lattice distortion. The blue and white dots denote sublattices A (with  $x+y$  odd) and B (with  $x+y$  even), and the gray dots denote the oxygens. The sign indicates the sign of the wave function in the positive  $z$  plane, and the wave functions in the negative  $z$  plane have opposite signs.

This lattice structure has an inversion symmetry  $\mathcal{I}$  with respect to site  $\vec{r}$ , and under such an inversion the orbitals transform as:

$$\begin{aligned} \mathcal{I} d_{s,a}^{xz}(\vec{r} \pm \hat{x}) \mathcal{I} &= d_{s,a}^{xz}(\vec{r} \mp \hat{x}) \\ \mathcal{I} d_{s,a}^{xz}(\vec{r}) \mathcal{I} &= d_{s,a}^{xz}(\vec{r}), \end{aligned} \quad (11)$$

with corresponding relations holding for the  $d_{s,a}^{yz}$  orbital. Therefore we have

$$\mathcal{I} d_{s,a}^{yz \dagger}(\vec{r}) d_{s,a}^{xz}(\vec{r} - \hat{x}) \mathcal{I} = d_{s,a}^{yz \dagger}(\vec{r}) d_{s,a}^{xz}(\vec{r} + \hat{x}). \quad (12)$$

The crystal also exhibits a reflection symmetry with respect to the  $yz$  planes containing the oxygen sites. Let us define  $\mathcal{J}$  as the reflection operation with respect to the  $yz$  plane containing the oxygen site between  $\vec{r}$  and  $\vec{r} + \hat{x}$ . Under the operation of  $\mathcal{J}$ ,

$$\begin{aligned} \mathcal{J} d_{s,a}^{xz}(\vec{r}) \mathcal{J} &= -d_{s,a}^{xz}(\vec{r} + \hat{x}) \\ \mathcal{J} d_{s,a}^{yz}(\vec{r}) \mathcal{J} &= +d_{s,a}^{yz}(\vec{r} + \hat{x}). \end{aligned} \quad (13)$$

Thus,

$$\mathcal{J} d_{s,a}^{yz \dagger}(\vec{r}) d_{s,a}^{xz}(\vec{r} + \hat{x}) \mathcal{J} = -d_{s,a}^{yz \dagger}(\vec{r} + \hat{x}) d_{s,a}^{xz}(\vec{r}), \quad (14)$$

Combining Eq.s 12 and 14 leads to:

$$\mathcal{J} \mathcal{I} d_{s,a}^{yz \dagger}(\vec{r}) d_{s,a}^{xz}(\vec{r} - \hat{x}) \mathcal{I} \mathcal{J} = -d_{s,a}^{yz \dagger}(\vec{r} + \hat{x}) d_{s,a}^{xz}(\vec{r}), \quad (15)$$

which means that this hopping is *staggered*.

Note that the above discussion is generally valid regardless of the intermediate state of the hopping process. The intermediate state, however, is important to give the second order perturbation expression for  $t_{\text{INT}}$  as

$$t_{\vec{r}\vec{r}'}^{\alpha\beta} = - \sum_m \frac{\langle \vec{r}, \alpha | H_{\text{RuO}} | m \rangle \langle m | H_{\text{RuO}} | \vec{r}', \beta \rangle}{E_d - E_m}, \quad (16)$$

where  $\alpha, \beta = xz, yz$ .  $H_{\text{RuO}}$  describes the hopping between the  $t_{2g}$  orbital on Ru sites and the  $2p$  orbitals on

neighboring O sites.  $|m\rangle$  denotes an oxygen  $2p$  orbital, which is an intermediate state for the Ru-Ru hopping processes. Because of the reflection symmetry with respect to the  $xy$  plane and the fact that  $d_{yz}$  and  $d_{xz}$  are odd under this reflection,  $\langle \vec{r}, \alpha | H_{\text{RuO}} | m \rangle$  is non-zero only if the intermediate state is also odd under this reflection. As a result,  $|m\rangle$  can be only  $|p_z\rangle$ . However, in order to determine the sign and the magnitude of  $t_{\text{INT}}$ , a detailed knowledge of the pseudopotentials for the Hamiltonian  $H_{\text{RuO}}$  is required, which is beyond the scope of this paper. Nevertheless, since this term is expected to be small

$$H_2^{\text{INTRA}} = -t_{\text{INT}} \sum_{\vec{r}, s, a, \hat{\delta}} (-)^a e^{i\vec{Q}\cdot\vec{r}} \left[ d_{s,a}^{yz\dagger}(\vec{r}) d_{s,a}^{xz}(\vec{r} + \hat{\delta}) - d_{s,a}^{xz\dagger}(\vec{r}) d_{s,a}^{yz}(\vec{r} + \hat{\delta}) \right] + \text{H.c.}, \quad (17)$$

where  $\hat{\delta}$  ranges over  $\hat{x}$  and  $\hat{y}$ ,  $(-1)^a = \mp 1$  for top and bottom layers, respectively, and where in our convention  $e^{i\vec{Q}\cdot\vec{r}} = \mp 1$  for  $\vec{r}$  in the A (B) sublattice. Note that there is only a single independent parameter  $t_{\text{INT}}$  to character-

and its main consequence is to provide the necessary coupling between  $\vec{k}$  and  $\vec{k} + \vec{Q}$ , where  $\vec{Q} = (\pi, \pi)$ , we can treat it as a fitting parameter.

Similar reasoning can be applied for the hybridized hopping between  $d_{xz}$  and  $d_{yz}$ -orbitals along the  $\hat{y}$ -direction, which is also staggered. Furthermore, the  $C_4$  symmetry around each Ru site relates the staggered hoppings along the  $\hat{x}$  and  $\hat{y}$ -directions. Putting all the above together, we arrive at the staggered in-plane hopping contribution to the Hamiltonian

ize this in-plane staggered hopping.

It is straightforward to transform Eq. 17 into momentum space as

$$H_2^{\text{INTRA}} = -2t_{\text{INT}} \sum'_{\vec{k}, s, a} (-)^a (\cos k_x + \cos k_y) \left[ d_{s,a}^{yz\dagger}(\vec{k} + \vec{Q}) d_{s,a}^{xz}(\vec{k}) - d_{s,a}^{xz\dagger}(\vec{k} + \vec{Q}) d_{s,a}^{yz}(\vec{k}) \right] + \text{H.c.}, \quad (18)$$

where the prime on the sum indicates that  $\vec{k}$  is restricted to only half of the Brillouin zone.

### C. Inter-layer staggered hopping

In this subsection, we study the additional hybridized inter-layer hopping between different orbitals, *i.e.*, the  $H_2^{\text{INTER}}$  term. This contribution arises because the rotation patterns of the RuO octahedra in the two layers are opposite to each other. Because the  $d_{xy}$  and  $d_{xz/yz}$  orbitals have different azimuthal quantum number of orbital angular momentum, they do not mix, even in the presence of the RuO octahedra rotation. The leading order inter-layer hybridization therefore occurs between  $d_{xz}$  and  $d_{yz}$  orbitals, and the hybridization Hamiltonian is

$$H_2^{\text{INTER}} = - \sum_{\vec{r}} e^{i\vec{Q}\cdot\vec{r}} \left[ t_{\text{bt}}^{(1)} d_{s,t}^{yz\dagger}(\vec{r}) d_{s,b}^{xz}(\vec{r}) + t_{\text{bt}}^{(2)} d_{s,t}^{xz\dagger}(\vec{r}) d_{s,b}^{yz}(\vec{r}) \right] + \text{H.c.} . \quad (19)$$

Next we use the second order perturbation theory to derive the staggered inter-layer hopping integrals. We

consider two hopping processes: (1) hopping from  $d_{xz}$  orbital at sublattice A on the bottom layer to  $d_{yz}$  orbital at sublattice B on the top layer, and (2) hopping from  $d_{yz}$  orbital at sublattice A on the bottom layer to  $d_{xz}$  orbital at sublattice B on the top layer. The hopping integrals for these two processes can be written as:

$$t_{\text{bt}}^{(1)} = - \sum_m \frac{\langle \vec{r}, yz, \text{b} | H_{\text{RuO}} | m \rangle \langle m | H_{\text{RuO}} | \vec{r}, xz, \text{t} \rangle}{E_d - E_m},$$

$$t_{\text{bt}}^{(2)} = - \sum_m \frac{\langle \vec{r}, xz, \text{b} | H_{\text{RuO}} | m \rangle \langle m | H_{\text{RuO}} | \vec{r}, yz, \text{t} \rangle}{E_d - E_m} \quad (20)$$

where  $i$  belongs to sublattice A in the bottom layer and sublattice B in the top layer by our convention. Because the  $d_{xz}$  and  $d_{yz}$  are odd under the rotation of  $90^\circ$  with respect to the  $z$  axis despite of the O-octahedral rotation, their overlaps with  $p_z$  are zero. Therefore the these two processes can only go through  $p_x$  and  $p_y$  orbitals of the oxygen between the layers. Fig. 4 presents the views of wavefunctions from the topview. It should be noted that for the top layer, the components of the wave functions having largest overlap with the oxygen  $p$  orbitals are the one in the negative  $z$  so that there is an additional minus sign in addition to those plotted in the Fig. 3. Unlike

the case of  $t_{\text{INT}}$ , because the Ru atoms on the top and bottom layers and the oxygen between them are colinear, the signs of  $t_{\text{bt}}^{1,2}$  can be determined from the geometry shown in Fig. 4. We can then obtain:

$$\begin{aligned} \langle \vec{r}, xz, \text{b} | H_{\text{RuO}} | p_x, 0 \rangle \cdot \langle p_x, 0 | H_{\text{RuO}} | \vec{r}, yz, \text{t} \rangle &> 0 \\ \langle \vec{r}, xz, \text{b} | H_{\text{RuO}} | p_y, 0 \rangle \cdot \langle p_y, 0 | H_{\text{RuO}} | \vec{r}, yz, \text{t} \rangle &> 0 \\ \langle \vec{r}, yz, \text{b} | H_{\text{RuO}} | p_x, 0 \rangle \cdot \langle p_x, 0 | H_{\text{RuO}} | \vec{r}, xz, \text{t} \rangle &< 0 \\ \langle \vec{r}, yz, \text{b} | H_{\text{RuO}} | p_y, 0 \rangle \cdot \langle p_y, 0 | H_{\text{RuO}} | \vec{r}, xz, \text{t} \rangle &< 0, \end{aligned}$$

where  $|p_x, 0\rangle$  is the oxygen  $2p_x$  orbital with planar position  $\vec{r}$  situated midway between the top (t) and bottom (b) ruthenium sites. Together with  $E_d - E_p > 0$ , we conclude that  $t_{\text{bt}}^{(1)} = -t_{\text{bt}}^{(2)} \equiv t_{\text{INT}}^\perp > 0$ . It can also be easily generalized that if  $\vec{r}$  belongs sublattice B (A) in the bottom (top) layer, we have obtain the same result except an opposite sign.

Now we transform into momentum space, after which the  $H_2^{\text{INTER}}$  term reads

$$H_2^{\text{INTER}} = -t_{\text{INT}}^\perp \sum_{\vec{k}}' \left[ d_{s,\text{t}}^{yz\dagger}(\vec{k} + \vec{Q}) d_{s,\text{b}}^{xz}(\vec{k}) - d_{s,\text{t}}^{xz\dagger}(\vec{k} + \vec{Q}) d_{s,\text{b}}^{yz}(\vec{k}) + d_{s,\text{b}}^{xz\dagger}(\vec{k} + \vec{Q}) d_{s,\text{t}}^{yz}(\vec{k}) - d_{s,\text{b}}^{yz\dagger}(\vec{k} + \vec{Q}) d_{s,\text{t}}^{xz}(\vec{k}) \right] + \text{H.c.} \quad (21)$$

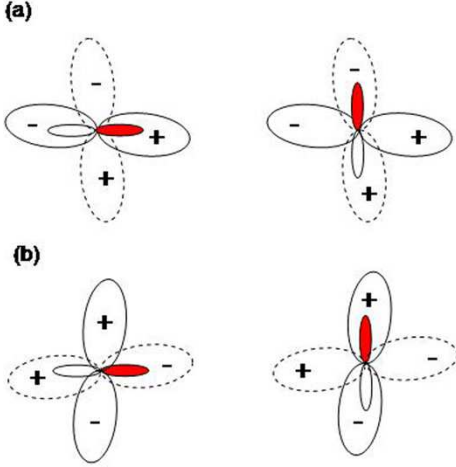


FIG. 4: (Color online) The wave functions viewed from the top of the material. The dashed line represents the wave function of the  $d$  orbitals on the top layer, and the solid line for those on the bottom layer. The smaller figures represent the  $p$  orbital of the oxygen between layers with the red lobe having positive sign and the white lobe having negative sign. Note that the signs of the  $d$  orbitals indicates those of the wave functions closest to the oxygen. (a)  $d_{xz}$  at bottom layer and  $d_{yz}$  at top layer, and (b)  $d_{yz}$  at bottom layer and  $d_{xz}$  at top layer.

#### D. Fermi surfaces

Adding up the contributions from Eqs. 5, 9, 18, and 21 leads to the tight-binding model

$$\begin{aligned} H_0 &= H_1^{\text{INTRA}} + H_1^{\text{INTER}} + H_2^{\text{INTRA}} + H_2^{\text{INTER}} \quad (22) \\ &= \sum_{\vec{k}}' \phi_{\vec{k},s}^\dagger \mathcal{H}_{\vec{k}} \phi_{\vec{k},s}, \end{aligned}$$

where

$$\mathcal{H}_{\vec{k}} = \begin{pmatrix} \hat{L}_s^+(\vec{k}) & -\hat{G}^\dagger(\vec{k}) & \hat{B}_1^\dagger & \hat{B}_2^\dagger \\ -\hat{G}(\vec{k}) & \hat{L}_s^+(\vec{k} + \vec{Q}) & \hat{B}_2^\dagger & \hat{B}_1^\dagger \\ \hat{B}_1 & \hat{B}_2 & \hat{L}_s^-(\vec{k}) & \hat{G}^\dagger(\vec{k}) \\ \hat{B}_2 & \hat{B}_1 & \hat{G}(\vec{k}) & \hat{L}_s^-(\vec{k} + \vec{Q}) \end{pmatrix}. \quad (23)$$

and

$$\phi_{\vec{k},s}^\dagger = (\psi_{s,\text{t}}^\dagger(\vec{k}), \psi_{s,\text{t}}^\dagger(\vec{k} + \vec{Q}), \psi_{s,\text{b}}^\dagger(\vec{k}), \psi_{s,\text{b}}^\dagger(\vec{k} + \vec{Q})), \quad (24)$$

with  $\psi_{s,a}^\dagger(\vec{k}) = (d_{s,a}^{yz\dagger}(\vec{k}), d_{s,a}^{xz\dagger}(\vec{k}), d_{s,a}^{xy\dagger}(\vec{k}))$  as before (see Eq. 5). The matrix kernels  $\hat{L}_s^a(\vec{k})$ ,  $\hat{G}(\vec{k})$ ,  $\hat{B}_1$ , and  $\hat{B}_2$  in Eq. 23 are defined as

$$\hat{L}_s^a(\vec{k}) = \hat{A}_s(\vec{k}) - (\mu - \frac{1}{2}(-1)^a V_{\text{bias}}) \hat{I}, \quad (25)$$

$$\hat{G}(\vec{k}) = \begin{pmatrix} 0 & -2t_{\text{INT}}\gamma(\vec{k}) & 0 \\ 2t_{\text{INT}}\gamma(\vec{k}) & 0 & 0 \\ 0 & 0 & 0 \end{pmatrix}, \quad (26)$$

and

$$\hat{B}_1 = \begin{pmatrix} -t_\perp & 0 & 0 \\ 0 & -t_\perp & 0 \\ 0 & 0 & 0 \end{pmatrix}, \quad \hat{B}_2 = \begin{pmatrix} 0 & t_{\text{INT}}^\perp & 0 \\ -t_{\text{INT}}^\perp & 0 & 0 \\ 0 & 0 & 0 \end{pmatrix}, \quad (27)$$

where  $\gamma(\vec{k}) = \cos k_x + \cos k_y$ ,  $\mu$  is the chemical potential, and  $V_{\text{bias}}$  is the difference of on-site potential in the top and bottom RuO layers. The  $V_{\text{bias}}$  term induces more splitting of bonding and anti-bonding solutions between layers, as will be discussed in the following sections.

For  $V_{\text{bias}} = 0$ ,  $H_0$  can be reduced to two independent parts classified by the bonding and anti-bonding solutions with respect to the layers. To see this, first we perform a gauge transformation in  $H_0$ , sending  $d_{s,\text{b}}^{yz,xz}(\vec{k} + \vec{Q}) \rightarrow -d_{s,\text{b}}^{yz,xz}(\vec{k} + \vec{Q})$ . Then we introduce  $k_z = 0, \pi$  to perform a Fourier transform on the layer index. We have:

$$H_0(V_{\text{bias}} = 0) = h_0(k_z = 0) + h_0(k_z = \pi), \quad (28)$$

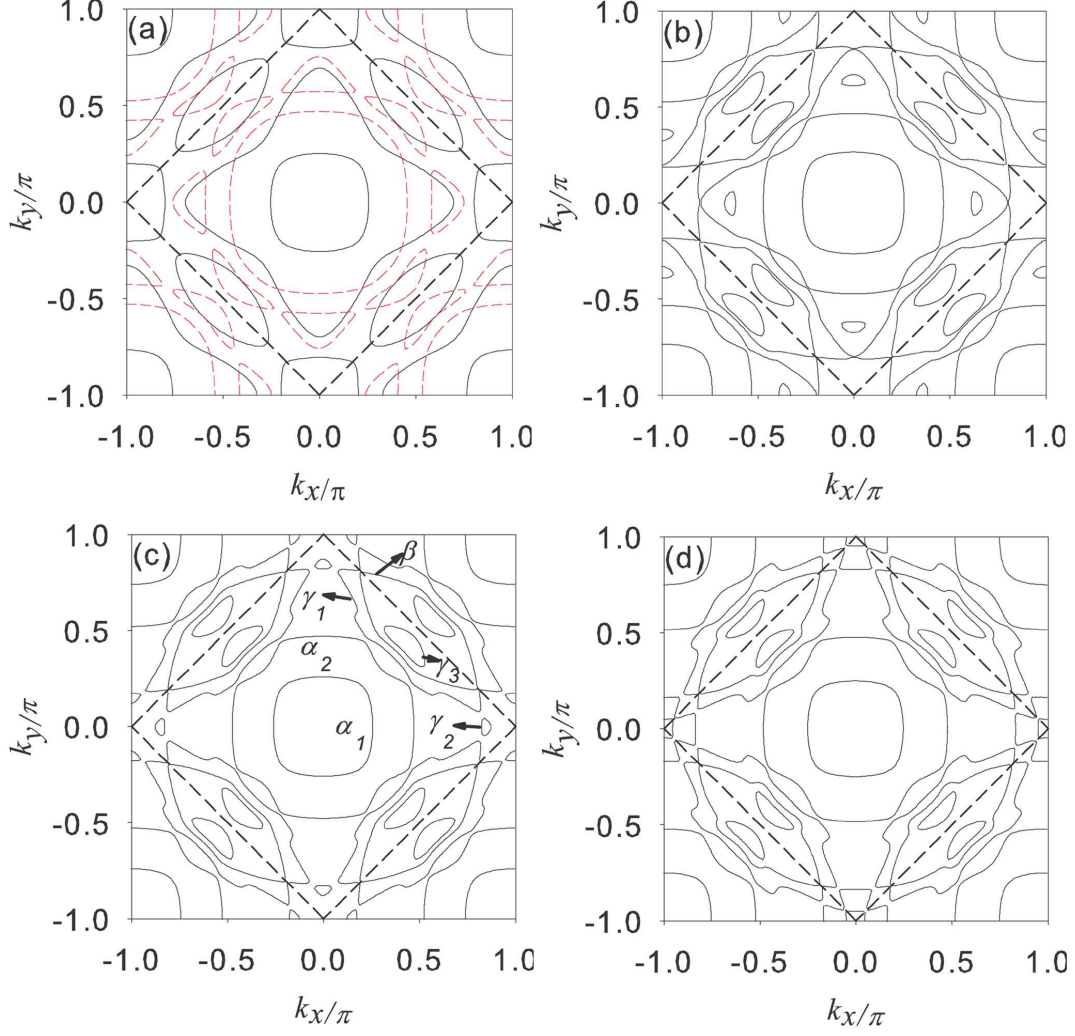


FIG. 5: (Color online) The Fermi surfaces using the bilayer tight-binding model with the parameters:  $t_1 = 0.5, t_2 = 0.05, t_3 = 0.5, t_4 = 0.1, t_5 = -0.03, t_6 = 0.05, t_\perp = 0.3, t_{\text{INT}} = t_{\text{INT}}^\perp = 0.05, \lambda = 0.1, V_{xy} = 0.15,$  and  $\mu = 0.47$  for (a)  $V_{\text{bias}} = 0,$  (b)  $V_{\text{bias}} = 0.1,$  (c)  $V_{\text{bias}} = 0.2,$  and (d)  $V_{\text{bias}} = 0.3.$  The thick dashed lines mark the boundary of half Brillouin zone due to the unit cell doubling induced by the rotation of octahedra oxygens. (a) For  $V_{\text{bias}} = 0,$  the Fermi surfaces of the bonding ( $k_z = 0,$  black solid lines) and the anti-bonding bands ( $k_z = \pi,$  red dashed lines) could cross since  $k_z$  is a good quantum number. (b) As  $V_{\text{bias}}$  is turned on, the crossings of the Fermi surfaces with different  $k_z$  are avoided. (c) The optimized Fermi surfaces are obtained with  $V_{\text{bias}} = 0.2.$  Fermi surface sheets of  $\alpha_1, \alpha_2, \gamma_1, \gamma_2, \gamma_3,$  and  $\beta$  are marked. The  $\gamma_{1,2}$  sheets have dominant 2-D  $d_{xy}$  orbital character while the  $\alpha_{1,2}$  sheets are mostly formed by quasi-1d  $d_{yz, xz}$  orbitals. The  $\gamma_3$  sheets are not seen in the ARPES measurements. (d) For  $V_{\text{bias}} = 0.3,$  the Fermi sheets of  $\gamma_2$  disappear.

with  $h_0(k_z)$  defined as

$$h_0(k_z) = \sum_{\vec{k}}' \Phi_{\vec{k}, s, k_z}^\dagger \begin{pmatrix} \hat{h}_{0s}(\vec{k}, k_z) & \hat{g}^\dagger(\vec{k}, k_z) \\ \hat{g}(\vec{k}, k_z) & \hat{h}_{0s}(\vec{k} + \vec{Q}, k_z) \end{pmatrix} \Phi_{\vec{k}, s, k_z}. \quad (29)$$

In Eq. 29,  $\hat{h}_{0s}, \hat{g}(\vec{k}, k_z)$  and  $\Phi_{\vec{k}, s, k_z}^\dagger$  are defined as

$$\begin{aligned} \hat{h}_{0s}(\vec{k}, k_z) &= \hat{A}_s(\vec{k}) + \hat{B}_1 \cos k_z \\ \hat{g}(\vec{k}, k_z) &= \hat{G}(\vec{k}) - 2\hat{B}_2 \cos k_z \end{aligned} \quad (30)$$

and

$$\Phi_{\vec{k}, s, k_z}^\dagger = \left( d_{\vec{k}, s, k_z}^{yz\dagger}, d_{\vec{k}, s, k_z}^{xz\dagger}, d_{\vec{k}, -s, k_z}^{xy\dagger}, \right. \\ \left. d_{\vec{k} + \vec{Q}, s, k_z}^{yz\dagger}, d_{\vec{k} + \vec{Q}, s, k_z}^{xz\dagger}, d_{\vec{k} + \vec{Q}, -s, k_z}^{xy\dagger} \right). \quad (31)$$

The Fermi surface for  $V_{\text{bias}} = 0$  is plotted in Fig. 5(a). It consists of many disconnected sheets. Since  $k_z$  is a good quantum number, the individual Fermi surfaces of the bonding and anti-bonding bands could cross; this in fact makes it easier to analyze how the Fermi surfaces are formed due to hybridization among the  $t_{2g}$  bands. It

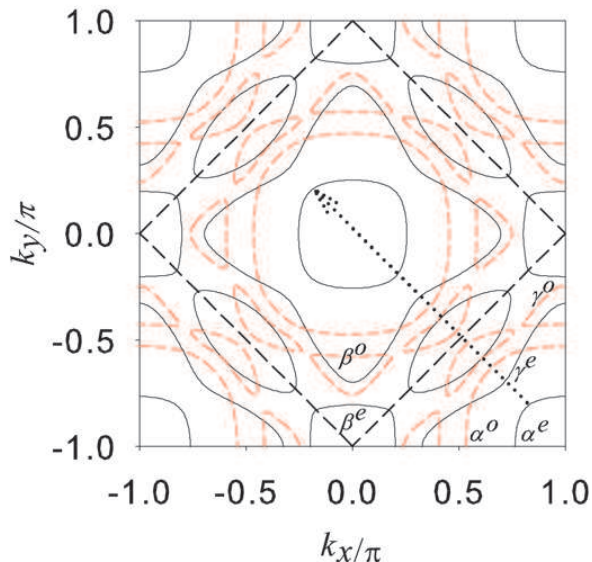


FIG. 6: (Color online) The analysis of the Fermi surface formation for  $V_{\text{bias}} = 0$ . Two copies of the Fermi surfaces of  $\text{Sr}_2\text{RuO}_4$  are labeled as  $\alpha^e$ ,  $\beta^e$ ,  $\gamma^e$  for bonding and  $\alpha^o$ ,  $\beta^o$ ,  $\gamma^o$  for anti-bonding bands. The back-folding of the Brillouin zone from the corners produces identical partners for each band appearing at positions connected by the wave vector  $\vec{Q} = (\pi, \pi)$  (the dotted arrow), leading to the Fermi surfaces plotted in Fig. 5(a).

has been illustrated in Ref. [68] that the Fermi surface of  $\text{Sr}_3\text{Ru}_2\text{O}_7$  can be schematically understood from that of  $\text{Sr}_2\text{RuO}_4$ . In  $\text{Sr}_2\text{RuO}_4$ , the hybridizations of the  $t_{2g}$  bands result in three eigenbands:  $\alpha$  and  $\beta$  bands with mostly quasi-1d  $d_{yz}$  and  $d_{xz}$  characters, and  $\gamma$  band with dominant  $d_{xy}$  character. For  $V_{\text{bias}} = 0$ , we can begin from two copies of the Fermi surfaces of  $\text{Sr}_2\text{RuO}_4$  since the bilayer splitting doubles for each band. From our calculations, three bonding bands ( $\alpha^e$ ,  $\beta^e$ , and  $\gamma^e$ ) and three antibonding bands ( $\alpha^o$ ,  $\beta^o$ , and  $\gamma^o$ ) are clearly identified, as shown in Fig. 6. Finally, due to the unit cell doubling induced by the rotated oxygen octahedra, the Brillouin zone is back-folded from the corners with respect to the dashed lines. As a result, each of the six bands will have an identical partner appearing at positions connected by the wave vector  $\vec{Q} = (\pi, \pi)$ , producing the Fermi surfaces plotted in Fig. 5(a).

When  $V_{\text{bias}} \neq 0$ , the crossings of the Fermi surfaces between bond and anti-bonding bands can be avoided because the  $V_{\text{bias}}$  term breaks the bilayer symmetry. To match the observed ARPES results<sup>52</sup>, it is crucial to avoid these crossings in order to obtain the correct shapes of the Fermi surface sheets. This suggests that a finite  $V_{\text{bias}}$  is a necessary aspect of any realistic model. Figs. 5(b)-(d) show the Fermi surfaces with several different value of  $V_{\text{bias}}$ , and it can be seen that the crossings of the Fermi surfaces are all avoided when  $V_{\text{bias}} \neq 0$ . Fig. 5(c) shows the Fermi surface with optimized parameters

fit to the ARPES experiment<sup>52</sup>. The agreement with experiment appears satisfactory. The Fermi surfaces of  $\alpha_1$ ,  $\alpha_2$ ,  $\gamma_1$ ,  $\gamma_2$ , and  $\beta$  identified from the ARPES are clearly reproduced with the correct shapes. Moreover, the average filling per Ru atom with these optimized parameters is 4.05, which is also consistent with the valence charge of Ru atoms in  $\text{Sr}_3\text{Ru}_2\text{O}_7$ .

One major discrepancy is the appearance of additional electron Fermi pockets,  $\gamma_3$ , enclosed by the  $\beta$  bands as shown in Fig. 5(c). While the LDA calculation also showed the existence of  $\gamma_3$  pockets, ARPES did not observe them. We suspect that this band might be too small to be resolved in the spectral weight measured by ARPES, and other measurements like quantum oscillations might be more sensitive to this band.

### III. T-MATRIX FORMALISM FOR THE MULTIBAND SYSTEMS

QPI imaging has been studied using a  $T$ -matrix formalism for various systems including the high- $T_c$  cuprates<sup>58,60</sup>, multiband systems with quasi-1d  $d$ -bands<sup>61</sup>, iron-pnictide superconductors<sup>69</sup>, and topological insulators  $\text{Bi}_2\text{Te}_3$ <sup>70,71</sup>, *etc.*. The scattering mechanism for the quasiparticles is usually taken to be elastic impurities, and is modeled by a local variation of the orbital energies. Because the impurities are introduced mainly on the surface of the material<sup>56</sup>, we consider a single impurity at  $\vec{r} = 0$  on the top layer only. Assuming that the impurity has the same effect for all orbitals, the impurity potential is modeled by

$$H^{\text{IMP}} = V_0 \sum_{\alpha} d_{s,t}^{\alpha\dagger}(\vec{r}=0) d_{s,t}^{\alpha}(\vec{r}=0), \quad (32)$$

where the orbital label  $\alpha$  runs over all three possibilities  $xy$ ,  $yz$ , and  $xz$ . In Fourier space, then,

$$\begin{aligned} H^{\text{IMP}} &= \frac{V_0}{N} \sum_{\vec{k}, \vec{k}', \alpha} d_{s,t}^{\alpha\dagger}(\vec{k}) d_{s,t}^{\alpha}(\vec{k}') \\ &= \frac{1}{N} \sum'_{\vec{k}, \vec{k}', s} \phi_{\vec{k}, s}^{\dagger} \hat{V} \phi_{\vec{k}', s}, \end{aligned} \quad (33)$$

where

$$\hat{V} = \begin{pmatrix} V_0 \hat{M} & \mathbb{O} \\ \mathbb{O} & \mathbb{O} \end{pmatrix}, \quad \hat{M} = \begin{pmatrix} \hat{I} & \hat{I} \\ \hat{I} & \hat{I} \end{pmatrix}, \quad (34)$$

with  $\hat{I}$  the  $3 \times 3$  identity matrix,  $\mathbb{O}$  is a  $6 \times 6$  matrix of zeroes, and where  $\phi_{\vec{k}, s}^{\dagger}$  is defined in Eq. 24.

Extending the standard  $T$ -matrix formalism to multiband systems<sup>61</sup>, we have that the Green's function satisfies the following matrix equation with dimension  $12 \times 12$ :

$$\hat{G}(\vec{k}, \vec{p}, \omega) = \hat{G}^0(\vec{k}) \delta_{\vec{k}, \vec{p}} + \hat{G}^0(\vec{k}) \hat{T}(\vec{k}, \vec{p}, \omega) \hat{G}^0(\vec{p}), \quad (35)$$

where  $\hat{G}^0(\vec{k})$  is the unperturbed Green's function defined as:

$$\hat{G}^0(\vec{k}) = \left[ \omega + i\eta - \hat{H}_0(\vec{k}) \right]^{-1} \quad (36)$$

and  $\hat{T}(\vec{k}, \vec{p}, \omega)$  is the  $T$ -matrix, which satisfies

$$\hat{T}(\vec{k}, \vec{p}, \omega) = \hat{V}(\vec{k}, \vec{p}) + \frac{1}{N} \sum'_{\vec{k}'} \hat{V}(\vec{k}, \vec{k}') \hat{G}^0(\vec{k}') \hat{T}(\vec{k}', \vec{p}, \omega) \quad (37)$$

Note that the momenta  $\vec{k}$  and  $\vec{p}$  are both restricted the half Brillouin zone. Since  $\hat{V}$  is momentum-independent, the  $T$ -matrix is also momentum-independent which can be easily evaluated as:

$$\hat{T}(\omega) = \left[ \hat{I} - \hat{V} \left( \frac{1}{N} \sum'_{\vec{k}'} \hat{G}^0(\vec{k}') \right) \right]^{-1} \hat{V}. \quad (38)$$

The local density of states (LDOS) on the layer  $a$  for orbital  $\alpha$ , spin  $s$  at position  $\vec{r}$  and sample bias voltage  $V$ ,  $\rho_{s,a}^\alpha(\vec{r}, E = eV)$  can be evaluated by:

$$\begin{aligned} \rho_{s,a}^\alpha(\vec{r}, E) = & \frac{1}{N} \sum'_{\vec{k}, \vec{p}} e^{i(\vec{p}-\vec{k}) \cdot \vec{r}} \left[ \mathcal{G}_{s,a}^\alpha(\vec{k}, \vec{p}, E) \right. \\ & \left. + \mathcal{G}_{s,a}^\alpha(\vec{k} + \vec{Q}, \vec{p} + \vec{Q}, E) \right] \\ & + e^{i(\vec{p}-\vec{k}-\vec{Q}) \cdot \vec{r}} \left[ \mathcal{G}_{s,a}^\alpha(\vec{k} + \vec{Q}, \vec{p}, E) \right. \\ & \left. + \mathcal{G}_{s,a}^\alpha(\vec{k}, \vec{p} + \vec{Q}, E) \right], \quad (39) \end{aligned}$$

where  $\mathcal{G}_{s,a}^\alpha(\vec{k}, \vec{k}', \omega) = \int dt e^{i\omega t} \langle T_t d_{k,s,a}^\alpha(t) d_{k',s,a}^{\alpha\dagger}(0) \rangle$  can be read off from Eq. 35. Generally speaking, the differential conductance  $dI/dV$  measured by the STM is proportional to the LDOS. However, special care must be taken in order to account for certain experimental details, as we will discuss in the following section.

## IV. RESULTS

### A. General discussions

First, it is important to mention that because experimentally the tip of the STM is much closer to the top layer, it predominantly measures the LDOS on the top layer. Second, because the wave functions for different orbitals could have different overlaps with the STM tip, the tunneling matrix elements may be orbital-dependent. Therefore, the simplest model to relate the conductance  $dI/dV$  and the corresponding LDOS can be written as:

$$\frac{dI}{dV}(\vec{r}, E) \propto \rho(\vec{r}, E) \equiv \sum_{\alpha,s} C^\alpha \rho_{s,t}^\alpha(\vec{r}, E). \quad (40)$$

Finally, the QPI imaging can be obtained by performing the Fourier transformation of  $\rho(\vec{r}, E)$ , *viz.*

$$\rho(\vec{q}, E) = \frac{1}{N} \sum_{\vec{r}} e^{-i\vec{q} \cdot \vec{r}} \rho(\vec{r}, E). \quad (41)$$

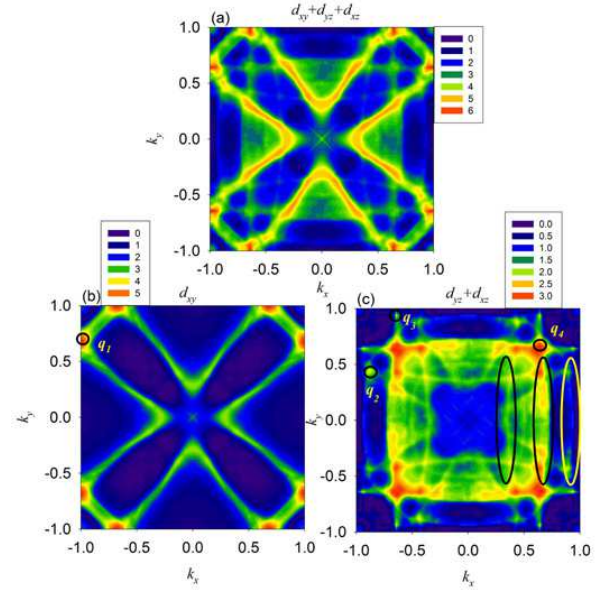


FIG. 7: (Color online) QPI imaging at zero sample bias voltage ( $E = 0$ ) contributed from scatterings (a) within all  $t_{2g}$  bands, (b) within 2-D band  $d_{xy}$ , and (c) within two quasi-1d bands  $d_{yz}$  and  $d_{xz}$ . The scattering potential is introduced only for top and bottom layers with  $V_0 = 1.0$ , reflecting the fact that the impurities are usually in the top layer. Only the LDOS on the top layer are calculated. (b) The strong features are due to the scatterings between the small hole pockets  $\gamma_2$  and the parts of  $\gamma_1$  marked by the solid lines in Fig. 8. A representative strongest wavevector  $\vec{q}_1$  is also indicated. (c) The strongest wavevectors  $\vec{q}_{2-4}$  can be understood by scatterings indicated in Fig. 8. The stripe-like features enclosed by the ovals (both black and yellow) result from the flat parts of the  $\alpha_{1,2}$  bands, which are the signatures of the quasi-1d bands.

In this paper, we plot  $|\rho(\vec{q}, E)|$  only for  $\vec{q} \neq 0$  since we are interested only in the change of the local density of states due to the impurity. A  $101 \times 101$  square lattice is used in the wavevector summations, and a broadening factor  $\eta = 0.02$  (*i.e.* an imaginary part to the energy) is introduced by hand.

We first compute the QPI imaging at zero sample bias voltage ( $E = 0$ ). Fig. 7(a) shows the QPI imaging due to impurity scattering from all three  $t_{2g}$  bands. The plot exhibits several features which can be understood as follows. Since the contributions to the LDOS from different  $t_{2g}$  bands can be computed independently as seen in Eq. 39, we also compute separately the QPI imaging for the 2-D  $d_{xy}$  band (Fig. 7(b)) and for the quasi-1d  $d_{yz}$  and  $d_{xz}$  bands (Fig. 7(c)) for comparison. The strong features seen in Fig. 7(b) come from the scatterings within and between  $\gamma_{1,2}$  pockets (the red solid lines in Fig. 8). This is to be expected, since both pockets have dominant  $d_{xy}$  orbital character. As for Fig. 7(c), the signature stripe-like patterns of the quasi-1d bands<sup>61</sup> can clearly be seen, and we find that the dominant features largely come from the  $\alpha_2$  band scatterings, as indicated in Fig. 8. The reason why the  $\alpha_2$  band scatterings are much

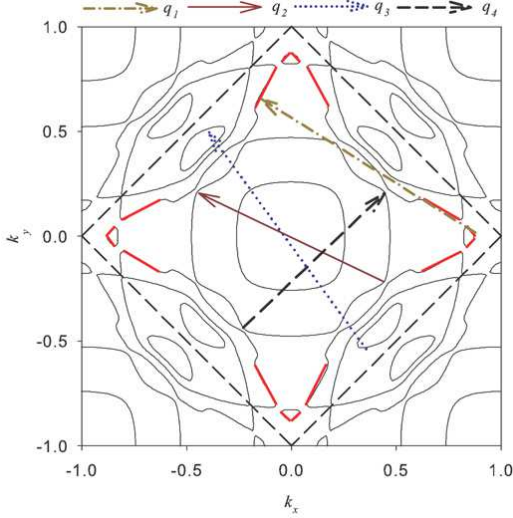


FIG. 8: (Color online) The scattering processes related to strongest features in Fig. 7. The scatterings within and between the parts of Fermi surfaces marked by the red solid lines, which are mostly from  $\gamma_1$  and  $\gamma_2$  pockets, contribute the dominant features in the QPI image of 2d band  $d_{xy}$  shown in Fig. 7(b). A representative strongest wavevector  $\vec{q}_1$  shown in Fig. 7(b) is plotted. As for the QPI image of quasi-1d bands  $d_{yz,xz}$  shown in Fig. 7(c), the dominant scatterings related to strongest wavevectors  $\vec{q}_{2-4}$  occur mostly within  $\alpha_1$  band, as indicated by the arrows.

more prominent than the  $\alpha_1$  band scatterings is that the  $\alpha_2$  ( $\alpha_1$ ) band is mostly composed of the anti-bonding (bonding) solution with respect to the layers, with more (less) weights on the top layer. Since we only compute the LDOS on the top layer, the  $\alpha_2$  band scatterings are much more important than the  $\alpha_1$  band scatterings.

Another general feature present in Figs. 7, also 10 and 11 is that while the Fermi surfaces without a nematic order have not only the  $C_4$  symmetry but also inversion symmetries with respect to  $k_x$  and  $k_y$  axes, the QPI patterns do not have the inversion symmetries with respect to  $q_x$  and  $q_y$  axes. The reason for this discrepancy is delicate, and we will explain in the following. As can be seen in Fig. 1, the inversion symmetry is defined only as the inversion axis chosen to pass through the oxygen sites. Since we have the degree of freedom to choose the inversion axis as computing the Fermi surfaces, Bloch theorem ensures that the system has the inversion symmetry. However, when computing QPI patterns, we have to put an impurity on one Ru site. As a result, we can only choose the inversion axis passing through this impurity at Ru site, which explicitly breaks the inversion symmetries. This explains why the QPI patterns do not have the inversion symmetries as the Fermi surfaces do.

It can be seen that Fig. 7(c) alone captures the main features of the experimental results of Ref. [56], suggesting that the contribution from the 2d  $d_{xy}$  band is essentially invisible in SI-STM experiment. The missing of  $d_{xy}$  band scatterings in the experiment can be

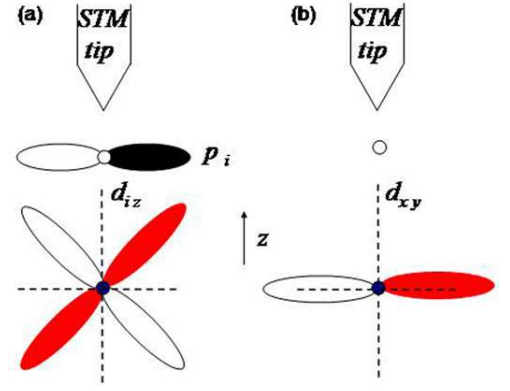


FIG. 9: (Color online) Schematic illustration of the wave function overlap related to the tunneling matrix element for STM tip. The tunneling of electrons from the STM tip to the  $d$ -orbitals of the Ru atoms must go through the oxygen atoms (white dots). (a) For  $d_{iz}$  orbitals ( $i = x, y$ ), the tunneling matrix element is large with the help of the  $p_i$  orbital of the oxygen atoms. (b) For  $d_{xy}$ , all  $p$ -orbitals of the oxygen atoms have zero wave function overlaps with it, leading to much weaker tunneling matrix element compared to  $d_{yz,xz}$  orbital.

explained by appealing to the aforementioned orbital-dependence of the STM tunneling matrix elements. Because the surface of the material is usually cleaved such that the outermost layer is the oxygen layer, there is an oxygen atom lying above each uppermost Ru atom. As a result, the tunneling matrix element will be mostly determined by the wavefunction overlaps between the  $p$ -orbitals of the oxygen atom and the  $d$ -orbitals of the Ru atom. As illustrated in Fig. 9, the wavefunction overlaps of the  $d_{yz}$  ( $d_{xz}$ ) orbital with the  $p_y$  ( $p_x$ ) are large while none of the  $p$ -orbitals has finite overlaps with  $d_{xy}$  orbital, leading to  $C^{xy} \ll C^{yz} = C^{xz}$ . Moreover, the tunneling matrix elements also depend on the in-plane momentum  $\vec{k}$ . It has been shown theoretically that the tunneling matrix elements have important effects in the tunneling spectra<sup>57,72-74</sup>. These matrix elements are significantly suppressed at large in-plane momentum<sup>72</sup>, and recent STM experiments on graphene<sup>74</sup> and iron-pnictide superconductors<sup>57</sup> have demonstrated this suppression. Since the  $\gamma_{1,2}$  sheets are located around momenta much larger than those of  $\alpha_{1,2}$ , their contributions could be further suppressed by this effect.

Based on the above discussion, we will henceforth set  $C^{yz} = C^{xz} = 1$  and  $C^{xy} = 0$ .

## B. QPI imaging at energy below the Fermi energy

Since the experiments were done at negative sample bias voltage<sup>56</sup>, we compute the QPI imaging for several negative values of  $E$ . Fig. 10 present the QPI imaging for  $E = 0, -0.03, -0.06, -0.1$ , and the main features of the stripe-like patterns remain unchanged. This is also consistent with the experiments showing that the QPI

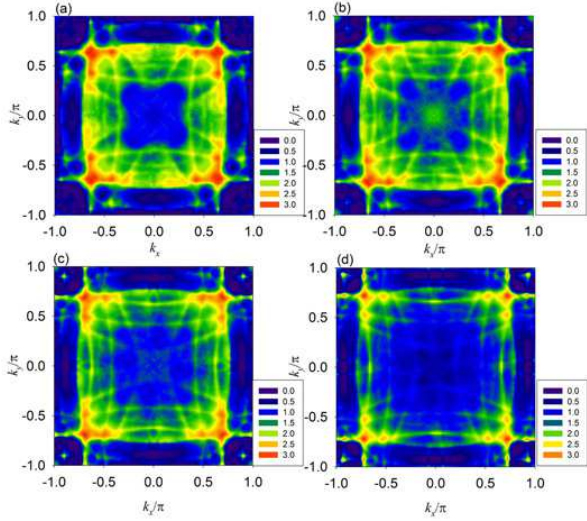


FIG. 10: (Color online) QPI imaging at (a)  $E = 0$ , (b)  $E = -0.03$ , (c)  $E = -0.06$ , and (d)  $E = -0.1$ . The main features are similar because the Fermi surfaces of  $\alpha_{1,2}$  are relatively insensitive to  $E$  throughout this energy range.

imaging are similar for sample bias voltage down to  $E = -12$  meV, and the reason is that the Fermi surfaces of  $\alpha_{1,2}$  do not change very much throughout this range of energy.

### C. QPI imaging for impurities at different layers

The above calculations were all performed assuming that the scattering impurity is located on the top layer only. However, QPI from impurity scattering in the second layer may also be detectable in experiments. Since the measurements of the conductance  $dI/dV$  are more likely an average of both cases, it is reasonable to expect

$$\frac{dI}{dV}(\vec{r}, E) \propto (1-x)\rho_{\text{TOP}}(\vec{r}, E) + x\rho_{\text{BOTTOM}}(\vec{r}, E), \quad (42)$$

where  $\rho_{\text{TOP}}(\vec{r}, E)$  is the LDOS of quasi-1d bands with impurity on the top layer, and  $\rho_{\text{BOTTOM}}(\vec{r}, E)$  is that with impurity on the bottom layer. We can then obtain the QPI imaging by performing a Fourier transformation on Eq. 42 as a function of  $x$ . The results are presented in Fig. 11 for  $x = 0.25, 0.5, 0.75, 1$ . We find that  $x = 0.25$  best reproduces the experimental data of Ref. [56].

## V. IMPLICATION OF ORBITAL ORDERING FROM QPI IMAGING

Two of us<sup>19</sup> have proposed that the nematic order observed in this material results from an orbital ordering in the quasi-1d bands enhanced by the orbital hybridizations. The charge and spin nematic order parameters  $n_c, n_{sp}$  can be expressed as:

$$n_c = \frac{1}{2}(\langle n_{xz} \rangle - \langle n_{yz} \rangle), \quad n_c = (\langle S_{xz}^z \rangle - \langle S_{yz}^z \rangle). \quad (43)$$

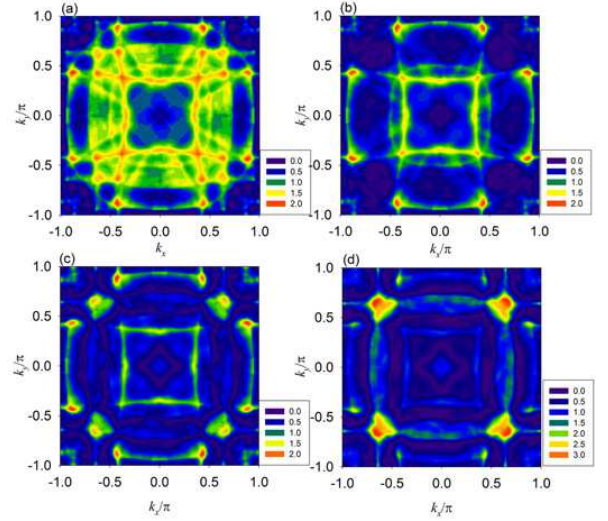


FIG. 11: (Color online) QPI imaging evaluated from Eq. 42 for (a)  $x = 0.25$ , (b)  $x = 0.5$ , (c)  $x = 0.75$ , and (d)  $x = 1$ . The QPI imaging in (a) fits the experimental result the best.

The mechanism of the nematic order under the magnetic field is that the majority spin band is pushed closer to the van Hove singularity, which triggers the nematic distortion in the majority spin Fermi surfaces. The mean field theory<sup>19</sup> with a microscopic model of quasi-1d bands also reproduced this feature, leading to  $n_c = n_{sp}$ . To calculate the QPI imaging with a nematic order, we introduce two new terms into the Hamiltonian:

$$H_{\text{nematic}} = N \sum_{\vec{r}, a} (d_{\uparrow, a}^{yz \dagger}(\vec{r}) d_{\uparrow, a}^{yz}(\vec{r}) - d_{\uparrow, a}^{xz \dagger}(\vec{r}) d_{\uparrow, a}^{xz}(\vec{r}))$$

$$H_{\text{Zeeman}} = -\mu_B B \sum_{\vec{r}, a, \alpha} (d_{\uparrow, a}^{\alpha \dagger}(\vec{r}) d_{\uparrow, a}^{\alpha}(\vec{r}) - d_{\downarrow, a}^{\alpha \dagger}(\vec{r}) d_{\downarrow, a}^{\alpha}(\vec{r})),$$

where  $N = n_c + n_{sp}$  measures the strengths of the nematic distortion in the majority spin Fermi surfaces. Fig. 12 shows the QPI imaging at  $E = 0$  with  $N/t_1 = 0.1$  and  $\mu_B B/t_1 = 0.06$ . As expected, a stripe-like pattern breaking the  $C_4$  symmetry down to  $C_2$  symmetry is observed.

We propose that this result could be used to resolve the controversy on which band is responsible for the nematic order. If the nematic order occurs mostly in the  $d_{xy}$  band and the quasi-1d bands do not exhibit orbital ordering, the QPI imaging from the experiments should have a  $C_4$  symmetry even within the range of the nematic order because the SI-STM is not sensitive to the  $d_{xy}$  band. Conversely, if the orbital ordering in the quasi-1d bands is responsible for the nematic phase, the SI-STM will see the imaging with only  $C_2$  symmetry, as shown in Fig. 12.

## VI. CONCLUSIONS

In this paper, we have constructed a bilayer tight-binding model with three  $t_{2g}$  orbitals for the  $\text{Sr}_3\text{Ru}_2\text{O}_7$ ,

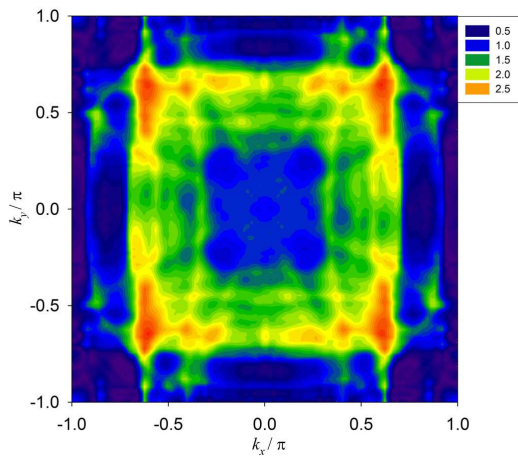


FIG. 12: (Color online) QPI imaging with nematic order.  $N/t_1 = 0.1$  and  $\mu_B B/t_1 = 0.06$  is chosen. The breaking of the  $C_4$  symmetry to  $C_2$  symmetry is clearly seen.

with careful attention paid to details of the lattice structure. We found that the rotations of the in-plane octahedra oxygens induce new hoppings between quasi-1d  $d_{yz}$  and  $d_{xz}$  bands with staggered signs in the hopping integrals, which in turn lead to a unit cell doubling consistent with what is observed in both ARPES experiment<sup>52</sup> and LDA calculations<sup>52,65</sup>. This mechanism for unit cell doubling is distinct from that in the model used by Puetter *et al.*<sup>55</sup>, in which a staggered on-site potential is introduced to distinguish the sublattices. Furthermore, we have also computed the quasi-particle interferences in the spectroscopic imaging STM based on a multiband  $T$ -matrix approach within this tight-binding model. Due to the effects of tunneling matrix elements, we find that the QPI imaging measured by Lee *et al.*<sup>56</sup> are dominated by the scatterings in the quasi-1d  $d_{xz}$  and  $d_{yz}$  bands, and the contribution from the 2-D  $d_{xy}$  band is largely suppressed. We have further considered the possibility of impurities residing on either top or bottom layers, and a linear combination of these two cases leads to the best fit with the experiments.

We have also calculated the QPI imaging for the system with an orbital ordering in the quasi-1d bands in a magnetic field, and we propose that this could be a realistic way to distinguish which band is responsible for the nematic order. We predict that if the  $d_{xy}$  band is the dominant band for the nematic phase and no orbital ordering in quasi-1d bands is present, the QPI imaging will still preserve the  $C_4$  symmetry even within the nematic phase because the SI-STM could not detect the change in the  $d_{xy}$  band. On the other hand, if the orbital ordering in quasi-1d bands is responsible, a breaking of the  $C_4$  symmetry down to  $C_2$  should be observed in the QPI imaging as the system enters the nematic phase.

One remarkable aspect in our tight-binding model is the introduction of  $V_{\text{bias}}$ , the difference in on-site potential for the top and bottom layers. It has been shown here that the crossings of the Fermi surfaces with different 'layer parities' can not be avoided without a  $V_{\text{bias}}$  term. In order to reproduce the Fermi surface sheets mapped out from the ARPES experiments, especially for  $\alpha_2$ , a non-zero  $V_{\text{bias}}$  is essential. Physically since the ARPES still measures mostly the electronic properties near the surface, it is reasonable to expect that the surface work function could produce a sizable  $V_{\text{bias}}$  to be seen in the ARPES. Furthermore, the fact that STM, another surface sensitive probe, detected only the  $\alpha_2$  band scatterings also supports the existence of a non-zero  $V_{\text{bias}}$ . On the other hand,  $V_{\text{bias}}$  vanishes inside the bulk, and thus the bulk Fermi surfaces would have different shapes and volumes from those obtained by ARPES<sup>52</sup>. This issue is important when comparing the Fermi surfaces measured in ARPES with those measured in quantum oscillations experiments, since the former is a surface measurement while the latter is a bulk one.

## VII. ACKNOWLEDGEMENT

We thank A. Mackenzie and J. C. Davis for helpful discussions. C. W. and W. C. L. are supported by ARO-W911NF0810291 and Sloan Research Foundation.

\* Electronic address: leewc@physics.ucsd.edu

† Electronic address: darovas@ucsd.edu

‡ Electronic address: wucj@physics.ucsd.edu

<sup>1</sup> M. Imada, A. Fujimori, and Y. Tokura, *Rev. Mod. Phys.* **70**, 1039 (1998).

<sup>2</sup> Y. Tokura and N. Nagaosa, *Science* **288**, 462 (2000).

<sup>3</sup> G. Khaliullin, *Prog. Theor. Phys. Suppl.* **160**, 155 (2005).

<sup>4</sup> D. I. Khomskii, *Physica Scripta* **72**, CC8 (2005).

<sup>5</sup> Y. Murakami, H. Kawada, H. Kawata, M. Tanaka, T. Arima, Y. Moritomo, and Y. Tokura, *Phys. Rev. Lett.* **80**, 1932 (1998).

<sup>6</sup> C. Ulrich, G. Ghiringhelli, A. Piazzalunga, L. Braicovich, N. B. Brookes, H. Roth, T. Lorenz, and B. Keimer, *Phys. Rev. B* **77**, 113102 (2008).

<sup>7</sup> H. Ichikawa, J. Akimitsu, M. Nishib, and K. Kakurai, *Physica B* **281-282**, 482 (2000).

<sup>8</sup> P. Khalifah, R. Osborn, Q. Huang, H. W. Zandbergen, R. Jin, Y. Liu, D. Mandrus, and R. J. Cava, *Science* **297**, 2237 (2002).

<sup>9</sup> T. Müller, S. Fölling, A. Widera, and I. Bloch, *Phys. Rev. Lett.* **99**, 200405 (2007).

<sup>10</sup> W. V. Liu and C. Wu, *Phys. Rev. A* **74**, 13607 (2006).

<sup>11</sup> C. Wu, B. A. Bernevig, and S. C. Zhang, *Phys. Rev. Lett.* **96**, 106401 (2006).

<sup>12</sup> C. Wu, *Phys. Rev. Lett.* **100**, 200406 (2008).

<sup>13</sup> C. Wu, *Phys. Rev. Lett.* **101**, 186807 (2008).

<sup>14</sup> C. Wu, *Mod. Phys. Lett. B* **23**, 1 (2009).

<sup>15</sup> W.-C. Lee, C. Wu, and S. D. Sarma, arXiv:0905.1146.

- <sup>16</sup> A.P. Mackenzie and Y. Maeno, *Rev. Mod. Phys.* **75**, 657 (2003).
- <sup>17</sup> I. Mazin and J. Schmalian, *Physica C* **469**, 614 (2009).
- <sup>18</sup> H. Zhai, F. Wang, and D.-H. Lee, *Phys. Rev. B* **80**, 064517 (2009).
- <sup>19</sup> W.-C. Lee and C. Wu, *Phys. Rev. B* **80**, 104438 (2009).
- <sup>20</sup> S. Raghu, A. Paramakanti, E. A. Kim, R. A. Borzi, S. A. Grigera, A. P. Mackenzie, and S. A. Kivelson, *Phys. Rev. B* **79**, 214402 (2009).
- <sup>21</sup> V. Oganesyan, S. A. Kivelson, and E. Fradkin, *Phys. Rev. B* **64**, 195109 (2001).
- <sup>22</sup> D. G. Barci and L. E. Oxman, *Phys. Rev. B* **67**, 205108 (2003).
- <sup>23</sup> M. J. Lawler, D. G. Barci, V. Fernandez, E. Fradkin, and L. Oxman, *Phys. Rev. B* **73**, 085101 (2006).
- <sup>24</sup> J. Nilsson and A. H. Castro Neto, *Phys. Rev. B* **72**, 195104 (2005).
- <sup>25</sup> J. Quintanilla and A. J. Schofield, *Phys. Rev. B* **74**, 115126 (2006).
- <sup>26</sup> C. J. Halboth and W. Metzner, *Phys. Rev. Lett.* **85**, 5162 (2000).
- <sup>27</sup> L. Dell'Anna and W. Metzner, *Phys. Rev. B* **73**, 045127 (2006).
- <sup>28</sup> H. Y. Kee, *Phys. Rev. B* **67**, 073105 (2003).
- <sup>29</sup> H. Yamase and A. Katanin, *J. Phys. Soc. Japan* **76**, 073706 (2007).
- <sup>30</sup> S. Kivelson, I. Bindloss, E. Fradkin, V. Oganesyan, J. Tranquada, A. Kapitulnik, and C. Howald, *Rev. Mod. Phys.* **75**, 1201 (2003).
- <sup>31</sup> C. M. Varma, *Philos. Mag.* **85**, 1657 (2005).
- <sup>32</sup> H.-Y. Kee and Y. B. Kim, *Phys. Rev. B* **71**, 184402 (2005).
- <sup>33</sup> C. Honerkamp, *Phys. Rev. B* **72**, 115103 (2005).
- <sup>34</sup> H. Yamase, V. Oganesyan, and W. Metzner, *Phys. Rev. B* **72**, 035114 (2005).
- <sup>35</sup> C. A. Lamas, D. C. Cabra, and N. Grandi, *Phys. Rev. B* **78**, 115104 (2008).
- <sup>36</sup> S. Kivelson, E. Fradkin, and V. Emery, *Nature* **393**, 550 (1998).
- <sup>37</sup> E. Fradkin and S. A. Kivelson, *Phys. Rev. B* **59**, 8065 (1999).
- <sup>38</sup> E. Fradkin, S. A. Kivelson, E. Manousakis, and K. Nho, *Phys. Rev. Lett.* **84**, 1982 (2000).
- <sup>39</sup> J. E. Hirsch, *Phys. Rev. B* **41**, 6820 (1990).
- <sup>40</sup> J. E. Hirsch, *Phys. Rev. B* **41**, 6828 (1990).
- <sup>41</sup> C. Wu and S.-C. Zhang, *Phys. Rev. Lett.* **93**, 036403 (2004).
- <sup>42</sup> C. Wu, K. Sun, E. Fradkin, and S.-C. Zhang, *Phys. Rev. B* **75**, 115103 (2007).
- <sup>43</sup> C. M. Varma and L. Zhu, *Phys. Rev. Lett.* **96**, 036405 (2006).
- <sup>44</sup> D. L. Maslov and A. V. Chubukov, *Phys. Rev. B* **81**, 045110 (2010).
- <sup>45</sup> S. A. Grigera, R. S. Perry, A. J. Schofield, M. Chiao, S. R. Julian, G. G. Lonzarich, S. I. Ikeda, Y. Maeno, A. J. Millis, and A. P. Mackenzie, *Science* **294**, 329 (2001).
- <sup>46</sup> S. A. Grigera, P. Gegenwart, R. A. Borzi, F. Weickert, A. J. Schofield, R. S. Perry, T. Tayama, T. Sakakibara, Y. Maeno, A. G. Green, and A. P. Mackenzie, *Science* **306**, 1154 (2004).
- <sup>47</sup> R. A. Borzi, S. A. Grigera, J. Farrell, R. S. Perry, S. J. S. Lister, S. L. Lee, D. A. Tennant, Y. Maeno, and A. P. Mackenzie, *Science* **315**, 214 (2007).
- <sup>48</sup> A. Berridge, A. Green, S. Gridera, and B. Simons, *Phys. Rev. Lett.* **102**, 136404 (2009).
- <sup>49</sup> A. M. Berridge, S. A. Grigera, B. D. Simons, and A. G. Green, *Phys. Rev. B* **81**, 054429 (2010).
- <sup>50</sup> A. J. Millis, A. J. Schofield, G. G. Lonzarich, and S. A. Grigera, *Phys. Rev. Lett.* **88**, 217204 (2002).
- <sup>51</sup> A. G. Green, S. A. Grigera, R. A. Borzi, A. P. Mackenzie, R. S. Perry, and B. D. Simons, *Phys. Rev. Lett.* **95**, 086402 (2005).
- <sup>52</sup> A. Tamai, M. P. Allan, J. F. Mercure, W. Meevasana, R. Dunkel, D. H. Lu, R. S. Perry, A. P. Mackenzie, D. J. Singh, Z.-X. Shen, and F. Baumberger, *Phys. Rev. Lett.* **101**, 026407 (2008).
- <sup>53</sup> K. Iwaya, S. Satow, T. Hanaguri, N. Shannon, Y. Yoshida, S. I. Ikeda, J. P. He, Y. Kaneko, Y. Tokura, T. Yamada, and H. Takagi, *Phys. Rev. Lett.* **99**, 057208 (2007).
- <sup>54</sup> C. Puetter, H. Doh, and H.-Y. Kee, *Phys. Rev. B* **76**, 235112 (2007).
- <sup>55</sup> C. M. Puetter, J. G. Rau, and H.-Y. Kee, *Phys. Rev. B* **81**, 081105(R) (2010).
- <sup>56</sup> J. Lee, M. P. Allan, M. A. Wang, J. Farrell, S. A. Grigera, F. Baumberger, J. C. Davis, and A. P. Mackenzie, *Nat. Phys.* **5**, 800 (2009).
- <sup>57</sup> T.-M. Chuang, M. P. Allan, J. Lee, Y. Xie, N. Ni, S. L. Bud'ko, G. S. Boebinger, P. C. Canfield, and J. C. Davis, *Science* **327**, 181 (2010).
- <sup>58</sup> A. V. Balatsky, I. Vekhter, and J.-X. Zhu, *Rev. Mod. Phys.* **78**, 373 (2006).
- <sup>59</sup> Y. Kohsaka, C. Taylor, P. Wahl, A. Schmidt, J. Lee, K. Fujita, J. W. Alldredge, K. McElroy, J. Lee, H. Eisaki, S. Uchida, D.-H. Lee, and J. C. Davis, *Nature* **454**, 1072 (2008).
- <sup>60</sup> Q.-H. Wang and D.-H. Lee, *Phys. Rev. B* **67**, 020511(R) (2003).
- <sup>61</sup> W.-C. Lee and C. Wu, *Phys. Rev. Lett.* **103**, 176101 (2009).
- <sup>62</sup> H. Shaked, J. D. Jorgensen, O. Chmaissem, S. Ikeda, and Y. Maeno, *J. Solid State Chem.* **154**, 361 (2000).
- <sup>63</sup> A. Liebsch and A. Lichtenstein, *Phys. Rev. Lett.* **84**, 1591 (2000).
- <sup>64</sup> I. Eremin, D. Manske, and K. Bennemann, *Phys. Rev. B* **65**, 220502(R) (2002).
- <sup>65</sup> D. J. Singh and I. Mazin, *Phys. Rev. B* **63**, 165101 (2001).
- <sup>66</sup> M. W. Haverkort, I. S. Elfimov, L. H. Tjeng, G. A. Sawatzky, and A. Damascelli, *Phys. Rev. Lett.* **101**, 026406 (2008).
- <sup>67</sup> M. H. Fischer and M. Sigrist, *Phys. Rev. B* **81**, 064435 (2010).
- <sup>68</sup> J. F. Mercure, A. W. Rost, E. C. T. O'Farrell, S. K. Goh, R. S. Perry, M. L. Sutherland, S. A. Grigera, R. A. Borzi, P. Gegenwart, A. S. Gibbs, and A. P. Mackenzie, arXiv:0909.1215.
- <sup>69</sup> Y.-Y. Zhang, C. Fang, X. Zhou, K. Seo, W.-F. Tsai, B. A. Bernevig, and J. Hu, *Phys. Rev. B* **80**, 094528 (2009).
- <sup>70</sup> W.-C. Lee, C. Wu, D. P. Arovas, and S.-C. Zhang, *Phys. Rev. B* **80**, 245439 (2009).
- <sup>71</sup> X. Zhou, C. Fang, W.-F. Tsai, and J. Hu, *Phys. Rev. B* **80**, 245317 (2009).
- <sup>72</sup> J. Tersoff and D. R. Hamann, *Phys. Rev. Lett.* **50**, 1998 (1983).
- <sup>73</sup> C. Wu, T. Xiang, and Z. B. Su, *Phys. Rev. B* **62**, 14427 (2000).
- <sup>74</sup> Y. Zhang, V. W. Brar, F. Wang, C. Girit, Y. Yayon, M. Panlasigui, A. Zettl, and M. F. Crommie, *Nat. Phys.* **4**, 627 (2008).